High-speed imaging of wave modes in an RDC

M.D. Bohon[a,*], R. Bluemner[a], C.O. Paschereit[a], E.J. Gutmark[b]

[a] *Chair of Fluid Dynamics, Technische Universität Berlin, 10623 Berlin, Germany*
[b] *Department of Aerospace Engineering, University of Cincinnati, Cincinnati, OH 45220, United States*

ABSTRACT

Various operating modes have been observed in the rotating detonation combustor (RDC) studied here, as well as by others. These modes can be generally categorized into two groups: one or more co-rotating waves and counter-rotating waves. The combustor is able to stabilize both types of operation, however the stabilization mechanism remains unclear. In order to better understand these cases, these operational modes are investigated with high-speed pressure transducers installed in the combustor annulus combined with simultaneous high-speed video imaging of the natural luminosity of the detonation wave from the aft end of the RDC. These results confirm the operation in both the steady single wave mode as well as the counter-rotating waves mode. The presence of this mode further demonstrates the complex dynamics inherent in the stabilization of the detonation wave. As each wave propagates, they initially begin to weaken followed by re-strengthening after collision which serves to stabilize the mode. Differences in the velocities of the waves was also observed to result in a beating phenomenon expressed as an amplitude modulation of the pressure traces. High-speed video imaging of the high-temperature emission from H_2O in the RDC annulus was used in conjunction with the pressure traces for a range of flow rates and equivalence ratios. Processing of the images into the wave frame of reference allowed for the identification of the average luminosity profile, characterized by a steep increase in natural luminosity near the wave front, followed by a trailing tail extending approximately half the annulus perimeter.

1. Introduction

After decades of research, constant pressure combustion systems are becoming increasingly difficult to realize significant improvements in efficiency. One solution to increasing efficiency is the use of Pressure Gain Combustion (PGC), of which Rotating Detonation Combustors (RDC) have emerged as a promising candidate. RDCs are typically composed of a closed-loop annular combustion chamber, around which a continuous detonation wave propagates. The detonation wave is self-sustaining through the continuous inflow of reactants from the head end of the combustor. The leading shock of the detonation wave results in a large increase in temperature, density, and pressure. The subsequent combustion drives the shock forward while the heat release results in a further increase in temperature and decrease in pressure and density. Compared to deflagration however, the net change in pressure across the detonation wave is positive while the entropy generation is reduced. This results in the potential for significant theoretical gains in thermal efficiency.

One of the hurdles to RDC operation is the extremely short time available for the replenishing of reactants. With operation typically in the kilohertz ranges due to the higher velocity of the detonation wave,

refill times for reactants are on the order of 100–500 μs. Injection of premixed reactants allows for the elimination of the time required for reactants to mix, and several attempts have been made to test premixed injection schemes in RDCs [1–3]. However, the inherent risk of flashback in such schemes has resulted in greater consideration being given to the separate injection of fuel and oxidizer. In order to reduce the coupling between the high pressure after the passage of the detonation wave with pressure feedback or back flow of products in the supply plenum [4], as well as to reduce the refill time, reactants are typically injected at or near choked conditions. Despite high reactant inflow velocities and supply plenum pressures, adequate mixing remains a challenge to RDC operation.

In well mixed, undisturbed reactants, a detonation wave will propagate at a fixed velocity relative to the speed of sound in the products [5]. This velocity, known as the upper Chapman-Jouguet (CJ) condition, is solely a function of the properties of the unburned mixture (temperature, pressure, mixture fraction, etc.). However in most experimental RDC studies, wave velocities significantly below the CJ velocity are measured. This effect is often attributed to either geometric interference [6] or poor reactant mixing [7–9]. Bykovskii et al. [10,11] found that insufficient mixing limits the regime for successful RDC

operation. In this study, they observed a retarded pulsed combustion front lagging a leading shock for low reactant flow rates, pressures, as well as for subsonic air injection. Alternatively, very stable detonations were observed for a wide range of conditions where high-quality mixing was achieved. Kindracki et al. [12] also observed unstable detonation propagation as a consequence of insufficient mixing. They observed reductions in the peak pressure and wave velocity with poor reactant mixing, which ultimately increased the detonation revolution lap time. Consequently, subsequent laps were allowed extra time for reactant mixing resulting in an increase in the detonation properties. This process then repeated between laps. The authors concluded care must be taken in the selection of the combustor geometry, reactant flow rates, and combustor annulus pressure as each of these parameters play an important role in the quality of reactant mixing.

Several numerical studies have investigated the reactant injection process. Schwer and Kailasanath [4] observed the coupling of the high-pressure products of detonation with the supply plenum. While back-flow of products was not observed, they did observe a significant feedback into the plenum with lower injection pressures. Frolov et al. [13] presented the first three-dimensional numerical simulation of RDC operation with separate reactant injection and found good agreement with experiments in terms of reactant fill height ahead of the detonation wave. Driscoll et al. [14] numerically investigated the flow field and mixing mechanisms within the combustion annulus of an RDC for varying injector configurations and reactant mass flows. They found an optimum injection area ratio between fuel and oxidizer in terms of mixing performance, however these results are only applicable to the specific geometry under investigation. In another numerical study, they found that low flow velocities in the annulus lead to improved mixing due to longer residence times [15]. Gaillard et al. [16] compared three-dimensional numerical simulations of detonation propagation for premixed as well as separate injection of hydrogen and oxygen, either distributed uniformly or spaced discretely. They observed significant dilution of the fresh mixture by the remaining hot gases with up to one third of the injected mass being burned by deflagrative combustion when injecting the reactants premixed through discrete holes. However, the propagation speed of the detonation wave still remained close to the ideal speed. Using separate reactant injection resulted in poor mixing efficiency, as well as globally incomplete combustion due to severe reactant mixture stratification. In a numerical study, Nordeen et al. [17] described the failure of the detonation wave due to incomplete mixing and instability in the detonation front height. They also observed the detachment of the detonation wave from the injection face resulting in a weak, lifted detonation wave. This effect was also previously observed experimentally [11,18].

The establishment of the counter-rotating wave mode is often attributed, at least in part, to the injection geometry and reduced mixing quality. Initially, this mode was observed as a transient or unsteady mode [19,20], while others have observed this mode to be steady [21–23]. Counter-rotating operation is detectable by high speed pressure measurements as well as high speed imaging. Typically observed at lower flow rate conditions, the pressure signals show large peaks at the intersecting point and lower pressures away from the intersection [22,24,25]. The presence of counter-rotating waves has also been observed by high speed imaging of the natural luminosity from the aft end of the combustor [23]. Bennewitz et al. [26] were able to observe multiple pairs of counter-rotating waves in a model rocket RDE while Chacon et al. [21] also observed this operating mode in a race track (obround) configuration.

Experimental investigations in the mixing region are more difficult to conduct, however several studies exist in the literature. Using an optically accessible RDC, the OH*-chemiluminescence in the detonation front was investigated with various injection geometries by Rankin et al. [27,28]. Depending on the injection geometry used, significant differences in both the wave shape and wave height, as well as the operating mode (i.e. number of simultaneously propagating waves),

were observed. In cases with poor reacting mixing, they also observed an unsteady operating mode with two counter-rotating waves. Good qualitative agreement to these effects was observed by Cocks et al. [29] in a simulation of the non-premixed RDC. In the same optically accessible RDC, Rankin et al. [30] utilized acetone PLIF to visualize the reactant mixing. A recirculation zone with minimal fuel entrainment was observed in the corner between the outer wall and the fuel injector plate. Importantly, during combustor operation, blockage of the reactant injectors was observed during approximately 18–22% of the cycle due to the high pressures behind the detonation wave. During this part of the cycle, no additional reactants were injected.

Typically, a trade-off is required between improving the mixing of reactants and minimizing the pressure losses through the injection. As discussed above, researchers have typically observed a shift in the mode of operation as the total flow rate of reactants (and the presumed quality of mixing) is decreased. Reactant mixing can be improved through the balance of high injector pressures, smaller injection areas, higher injection velocities, and geometric features to enhance mixing (e.g. jets in crossflow, impinging jets, etc.). Additionally, decoupling the feedback into the reactant plena from the passage of the detonation wave is an important consideration for injector design. On the other hand, reducing the pressure drop across the injectors is an important requirement for practical PGC devices and requires a trade off with the aforementioned features. The consequence of reactant mixing quality is often directly observable in the mode of operation within the combustor. The objective of this work is therefore to observe the modes of operation of the RDC under variable qualities of reactant injection and observe how the properties of the detonation wave vary with different modes of operation. The combustor utilizes the often replicated radially-inward injection scheme [31] as a baseline against which future studies can be compared. The combined diagnostics of high-speed pressure transducers installed in the combustor annulus with high-speed imaging of the natural luminosity of the detonation wave allow for a direct study of the RDC operational mode.

2. Experimental setup

The RDC used in this study is based on a design, developed by the US Air Force Research Lab (AFRL) [31], which utilizes a radially inward configuration for the oxidizer injection. Shown in Fig. 1, oxidizer (O) is injected through a continuous slot at the base of the combustor that extends around the outer circumference of the annulus, as indicated by the blue arrows. The combustor annulus has an outer diameter of $D = 90$ mm. The oxidizer injection slot has a variable injection height of $g = 1$ or 1.6 mm. This work presents results using the 1.0 mm injector configuration, resulting in an oxidizer injector area of $A_o = 282.4$ mm^2. Fuel is injected through a total of $N = 100$ holes, with a diameter of $d = 0.5$ mm each, equally spaced around the circumference of the outer wall. This results in a total fuel injection area of $A_f = 19.6$ mm^2. Table 1 shows a summary of the relevant geometry of the combustor. The fuel jets and cross-flowing oxidizer are configured in a jet-in-crossflow situation as shown in Fig. 1(a). Positioning of the fuel injection configuration is also variable through changeable fuel injector plates, with the standard configuration chosen such that the fuel injector holes are positioned tangentially to the outer-wall circumference, with the center of the injector inside the outer wall diameter. In each configuration, the local blowing ratio is expected to impact the mixing of reactants dependent upon the impingement of the fuel jet on the oxidizer slot confinement. In this work, the combustor annulus width is fixed at a value of $\Delta = 7.6$ mm, resulting in a mean annulus perimeter of $P_m = 258.9$ mm.

The mass flow rates of reactants are controlled by regulating the flow through a pair of sonic nozzles (one for fuel and another for oxidizer). Static pressure transducers and RTDs record the pressures and temperature upstream of the sonic nozzles as well as the conditions in the injector plena within the RDC. Precise flow rate control is achieved
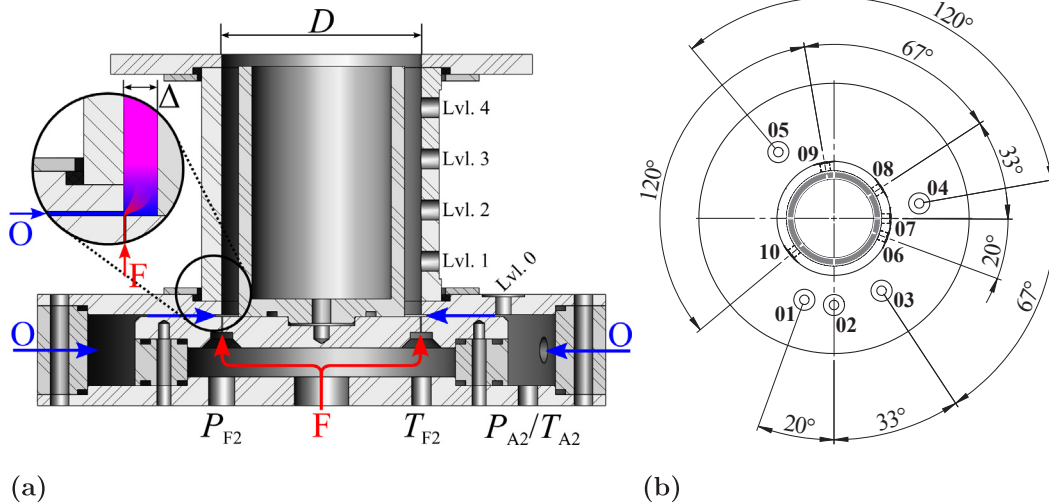
Fig. 1. (a) Cross section of the RDC, indicating the modular fuel (F, in red) and oxidizer (O, in blue) injection scheme, the static temperature T and pressure P ports, annulus width Δ, combustor outer diameter D, as well as the different instrumentation port elevations ranging from level 0 in the oxidizer injection slot to level 4 just upstream of the RDC exhaust. (b) Aft end view of the RDC, indicating the circumferential spacing and numbering of the instrumentation ports, with five ports in the oxidizer injection slot (01–05) and five ports in the first level of the annulus (06–10). (For interpretation of the references to colour in this figure legend, the reader is referred to the web version of this article.)

Table 1
Relevant RDC geometry dimensions.

Property	Value
Fuel injection area, A_f	19.6 mm^2
Oxidizer injection area, A_o	282.4 mm^2
Annulus outer diameter, D	90 mm
Annulus width, Δ	7.6 mm
Mean annulus perimeter, P_m	258.9 mm
Oxidizer slot height, g	1.0 mm
Fuel hole diameter, d	0.5 mm
Number of fuel holes, N	100

by regulating an electronically controlled pilot regulator supplying set point pressures to dome-loaded pressure regulators responsible for controlling the bulk flow. With this work, all experiments presented use compressed air and hydrogen for reactants. A nominal continuous flow of air purges the combustor before and after test runs. A fast-acting, pneumatically actuated solenoid valve located immediate before the fuel plenum serves to control the on/off supply of fuel to the combustor. Each test run is controlled by a prescribed run scheme in which target reactant supply pressures are set, along with all timing and/or triggered events. All experimental conditions and data points are recorded using a 500 kHz data acquisition system.

As neither the outer body nor the center body of the RDC were cooled, test runs were limited to a relatively short duration with purging air flow providing cooling between runs. Each test period began with the ramping up of the oxidizer flow to the target value. After stabilizing (approximately $\Delta t < 1s$), the fuel flow was ramped up to its corresponding target depending on equivalence ratio. Simultaneously, the pneumatically actuated shut off valve was opened. Following stabilization of the reactant flow rate and filling of the combustion chamber, the RDC was ignited by a flush-mounted automotive spark plug. The spark plug was positioned at the base of the combustion annulus. After ignition, the flame was allowed to transition to detonation naturally, which typically occurred quickly and stabilized within the first 25–50 ms. The supply of reactants continued for the test duration, after which the pneumatically actuated shut-off valve closed, stopping the supply of fuel. The supply of oxidizer was then reset to the idle flow rate to provide purging of the combustor.

The outer body of the RDC can be equipped with a wide array of

instrumentation. Ports are distributed circumferentially and axially. In this work, five un-cooled piezoelectric charge mode pressure sensors, model PCB 112A05, were flush-mounted in the outer wall of the combustor (locations [06-10] in Fig. 1(b)) near the base of the combustor annulus (level 1 in the same figure). The spacing of sensors in each level was configured in two different patterns. The first pattern follows a uniform spacing of 120° (ports [06,09,10]), while the second pattern utilizes a non-uniform spacing of 20°, 33°, and 66° ([06,07,08]). The non-uniform spacing and relatively close proximity of sensors allows for easier measurement of wave speed and direction, as well as the detection of multiple waves. To protect the sensors from excessive thermal loading, which may lead to signal saturation or catastrophic damage to the sensors, test durations were kept short, usually around 300 ms. It was observed that this time allowed for the dynamics of combustion to become relatively steady within the first 200 m/s, without damaging the sensors. In post processing, all PCB signals were high-passed filtered at 100 Hz cut-on frequency to remove the baseline thermal drift.

A high-speed camera (Photron SA-Z) imaged the annulus from the aft end, through the exhaust plume using a visible wavelength mirror. Images of the broad-band natural luminosity were recorded at a rate of $F_s = 87500$ frames per second, with an exposure time of $8.75\,\mu s$ and an inter-frame time of $11.4\,\mu s$. Images were constrained to a 200×200 pixel region, corresponding to approximately 2 pixels/mm. The combination of the visible wavelength mirror eliminating reflections in the UV and the limited sensitivity of the camera sensor to wavelengths above about 900 nm resulted in imaging primarily in the visible and near-IR spectrum. Imaging of the detonation wave enabled the time-resolved visualization of location, number, and direction of the waves within the annulus, as well as gaining clarity in evaluating instability phenomena. For a stoichiometric hydrogen-air mixture at normal temperature and pressure, a detonation wave propagates at a maximum velocity corresponding to the CJ velocity of approximately 1965 m/s. Such a wave would complete a single lap in the RDC annulus in approximately $132\,\mu s$ based on the mean perimeter. This corresponds to approximately 12 frames per lap and the advancement of the detonation wave of approximately 30° between frames. From observations, the detonation waves in the RDC travel at reduced speeds relative to the CJ velocity, effectively improving the angular resolution.

3. Results

The objective of this work is to investigate the features of several interesting modes of operation within the RDC, including highlighting observations on the dynamics of the stabilization of the detonation waves and applying novel techniques to the analysis of the operation. With this combustor configuration, two modes of operation are routinely achievable. The first is the canonical single wave mode. This mode was present for moderate-to-high flow rates over most equivalence ratios. Transition to a pair of co-rotating waves with increasing mass flow was not observed due to limited reactant flow rate capabilities in the laboratory. The second mode of operation was a pair of counter-rotating waves, which occurred for low-to-moderate flow rates over a wide range of equivalence ratios. These results will be discussed in two sections. The first section will investigate the pressure traces of sensors installed in the combustor annulus under two different conditions. Unique features of the operational modes will be discussed and recommendations for the identification of these modes provided. The second section will focus on analyzing the high-speed images of the aft end of the combustor, with the goal of confirming the observations from the pressure traces while also providing additional insights into the features of the propagation and interaction of these waves.

3.1. Pressure measurements in the annulus

The standard mode of operation in the RDC is presumed to be the stable single wave mode, propagating around the combustion annulus at a constant speed. An example of this mode of operation is shown in Fig. 2. Shown in this figure are three non-uniformly space PCB sensors located in level 1 of the detonation annulus. The run duration was limited to 300 ms, which was observed to be short enough to prevent damage to the flush-mounted sensors, but long enough to allow for the system to stabilize and the operating mode to become constant. This steadiness was confirmed in separate tests in which the PCBs in the combustion annulus were removed and the run duration was increased to four seconds. PCB pressure sensors in the air injector gap and high-speed video from the aft end of the combustor confirmed that beyond the initial stabilization period, the mode of operation did not change appreciably and that the transient initiation behavior was limited to the first 30–50 ms after ignition.

Fig. 2a shows a 20 ms subsection of the total test duration for an air

mass flow rate of 0.35 kg/s and a nearly stoichiometric equivalence ratio of $\phi = 0.98$. The variation in the magnitude of the peak height from subsequent wave passages around 4 bar shows a stochastic variation, with no clear modulating frequency. Zooming in further, Fig. 2b shows the passage of several consecutive wave passages. The relatively close and non-uniform sensor spacing provides a clear indication of the wave propagation in the clockwise direction. Lastly, a short time FFT of one of the PCBs can be seen in Fig. 2c. This FFT was determined from a sliding interrogation window with a length of approximately 10 ms and a 50% overlap. This length window represents a compromise between temporal resolution and frequency resolution, which is limited to approximately 100 Hz (corresponding to uncertainty in the wave speed of ± 30 m/s). From this figure, one can observe the establishment of a steady, single, dominant frequency around 5775 Hz which corresponds to a wave speed of 1495 m/s at the mean annulus perimeter P_m. Per NASA CEA [32], this operating condition should provide an expected CJ velocity of 1956 m/s and a pressure ratio of 15.4. Therefore, the measured velocity corresponds to approximately 76% of the CJ velocity and is comparable with values measured by others in similar configurations [7]. At this operating frequency, the maximum fill height is estimated to be 26 mm, which is approximately at the position of the first row of PCB sensors at 25.6 mm. In actuality, the wave height is likely to be lower than this estimated height and consequently the sensor position may be too high to capture the maximum pressure rise through the detonation wave. Future iterations of the combustor will lower the position of the first row of sensors to improve the positioning relative to the detonation wave, however the current configuration is more than adequate to resolve the operational mode.

A more interesting mode of operation is shown in Fig. 3. For the same combustor geometry and approximately equal equivalence ratio at $\phi = 1.0$ but lower air mass flow rate of 0.14 kg/s, the steady mode of operation is much more complex. From Fig. 3a, it is immediately apparent that a strong amplitude modulation is occurring throughout the run. Such amplitude modulations have been observed by several other groups [33–35]. By examining the closely and non-uniformly spaced set of three sensors, as shown in Fig. 3b, the cause of this amplitude modulation becomes clear. This dynamic is explained by a pair of counter-rotating waves at similar but slightly different speeds. In this figure, a small shaded section shows the distinct passage of the clock-wise rotating wave indicated by the sequential blue-red-yellow (PCB 08-07-06). This wave passage is then immediately followed by a
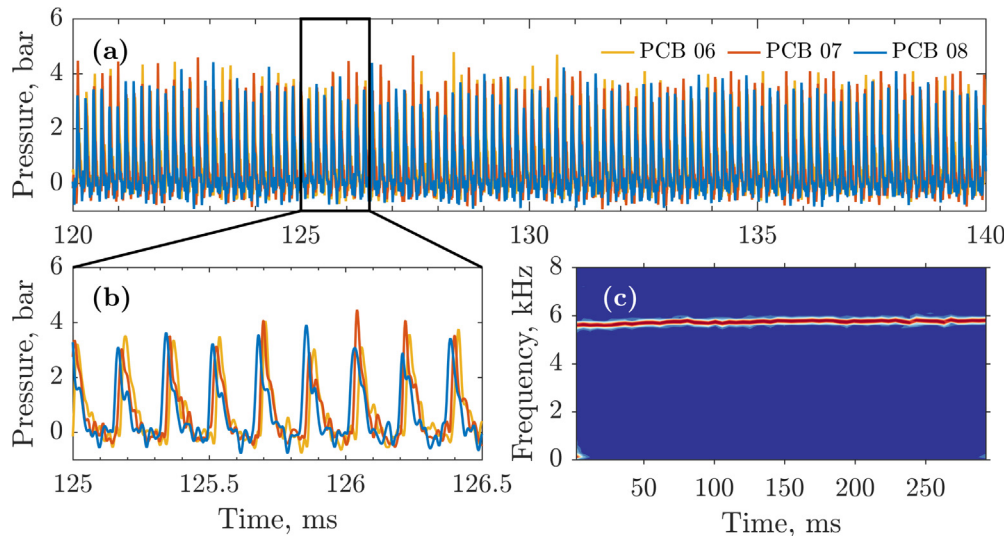

Fig. 2. Pressure traces of three non-uniformly spaced PCBs in level 1 of the annulus (refer to Fig. 1 for sensor locations) during stable single wave operation for an oxidizer mass flow of 0.35 kg/s and an equivalence ratio of $\phi = 0.98$. A sample pressure trace (a) showing the stochastic nature of pressure peak height is further magnified (b) highlighting the wave speed and clockwise direction. A short time FFT (c) with a sliding interrogation window of approx. 10 ms and a 50% overlap shows the establishment of a steady, single dominant frequency.
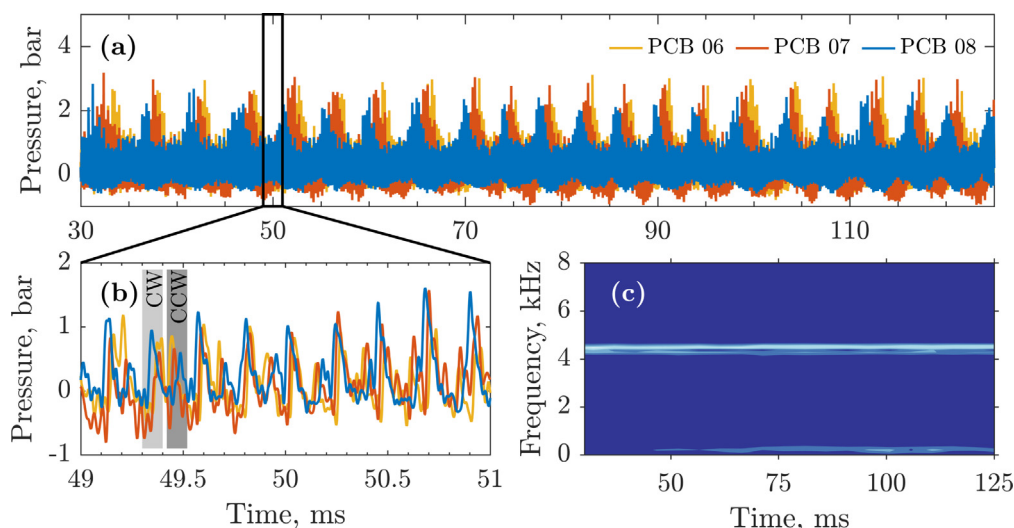
Fig. 3. Pressure traces for the same PCBs during operation with two stable counter-rotating waves for an oxidizer mass flow of 0.14 kg/s and an equivalence ratio of $\phi = 1.0$. A sample pressure trace (a) showing a strong amplitude modulation of the pressure peaks is further magnified (b) highlighting the presence of two counter-rotating waves traveling at slightly different speeds and strengths. A short time FFT (c) of the full run time shows the decreased overall operating frequency compared to one-wave operation, with two closely-spaced but separate frequency peaks.

second, counter-clockwise wave indicated by the reverse order. It is important to recognize that this analysis is only possible due to the close spacing of the sensors. It is necessary that the sensors be positioned close enough together to clearly observe the uninterrupted passage of an individual wave. Therefore, the sensor pair must span less than 90° or else it becomes impossible to definitively identify a set of peaks as occurring due to the passage of an individual wave.

These two waves do not propagate at the same speed, as indicated by the double peaks in the FFT shown in Fig. 3c around 4400 Hz (4472 and 4268 Hz for the primary and secondary waves, respectively). Because the two waves are at different speeds, the point at which they intersect will slowly shift around the combustor in the direction of the faster wave at a frequency equal to the difference of the two wave frequencies of 204 Hz in this example. As the position of the sensor is static, this shifting intersection point will result in the time between successive wave passages decreasing as the intersection point approaches and then increasing again as the intersection continues around the combustor. Additionally, when the intersection point overlaps the sensor, the interacting waves result in the significant increase in the measured pressure and this interaction yields the lower frequency modulation of the peak pressure observed in Fig. 3a.

One can also observe that the order of the amplitude modulation is indicative of the direction of travel of the wave intersection point. The wave pair shows a blue-red-yellow (PCB 08-07-06) order, indicating that the intersection point is rotating in the clockwise direction. This is also consistent with the faster and higher pressure wave moving in the clockwise direction as observed in Fig. 3b. In this case, the direction of the faster wave is consistent throughout the course of the run. However, in other similar cases, it was also observed that the order of amplitude modulation may suddenly switch direction, indicating that the stronger wave can sporadically reverse directions. This swapping of wave direction can also occur multiple times in the course of a run, and no preferential direction was observed. In the short-time FFT, there is no indication of these wave reversals, however in examining the temporally resolved FFT one is always able to observe two distinct peaks (assuming adequate spectral resolution), regardless of which direction the dominant wave is rotating. In the case presented here, the frequencies correspond to velocities of 1157 and 1104 m/s, or 59% and 56% of the CJ velocity, which is on the low range of detonation wave speeds measured. The stabilization mechanism for this mode of operation remains unclear, however one could reasonably speculate that

the renewal of the detonation wave or local explosion at the crossing point of the counter-rotating waves plays a role in stabilizing the combustion. There is also a strong coupling between the flame, the reactant injector stiffness, and the reactant mixing. Investigating how these parameters interact with the stabilization of the counter-rotating waves is the focus of further work and is outside the current scope, however how these two wave interact will be of interest in the following section in the analysis of the high-speed imaging from the aft end of the combustor.

3.2. High-speed imaging of the RDC annulus

Simultaneously with the pressure measurements in the combustor annulus, high-speed imaging of the natural luminosity of the H_2-air combustion from the aft end of the combustor was conducted. Still frames from this high-speed imaging for the two modes of operation discussed above are shown in Fig. 4. The luminosity imaged in each frame is the result of broad-band emission of high-temperature H_2O in the yellow-red and near-IR spectrum [36]. While the broadband emission intensity is non-linear in temperature, which makes quantification and direct comparison between cases difficult, it does serve to show the high-temperature regions behind the detonation wave. The images were captured using a generic glass mirror located in the RDC exhaust, however the glass overlay was not transparent to emission from OH^* in the UV region. Therefore, this additional emission source was not imaged on the camera sensor. Additionally, since the camera's line of sight images through the length of the entire combustor, the luminosity shown in the images is the result of integrating through the entire exhaust plume which limits the resolution of small scale features.

In these snapshot images, the arrows indicate the location and direction of wave propagation, while the temporal progression is from left to right. The set of images in the top row shows a single detonation wave propagating in the clockwise direction around the RDC annulus and corresponds to the run shown in Fig. 2. The time series in these images spans a total of 183 μs. Throughout the combustion run, the luminosity in the leading edge remains nearly constant followed by a trailing region of decreasing luminosity. The second row in Fig. 4 shows a pair of counter-rotating waves spanning 137 μs. Due to the weaker mode of operation as discussed previously, the luminosity in the flame front was very low and results in a noisier image. In the time series, from left to right, the two waves separate and propagate in opposite
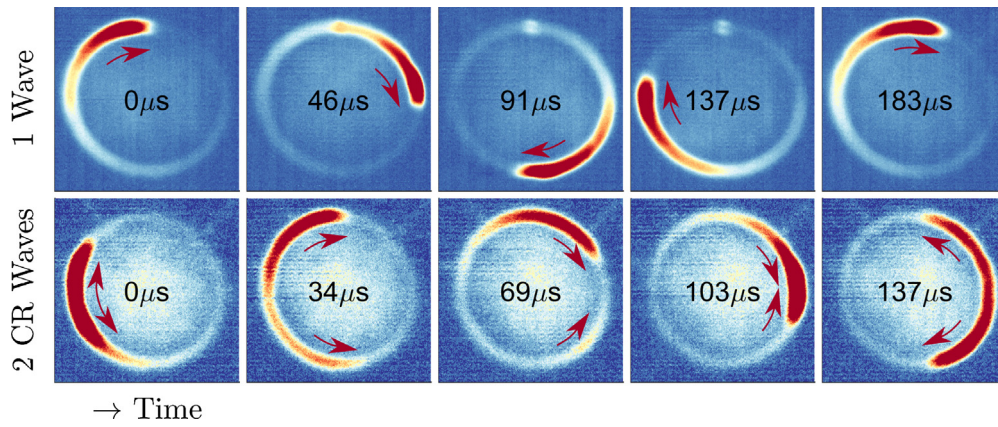
Fig. 4. Selected raw data snapshots of luminosity within the annulus imaged from the aft end of the RDC, showing one wave propagating clockwise at the top, and two counter-rotating waves at the bottom propagating in a clapping mode.

directions around the combustor. After separating, both waves decrease in luminosity throughout the half-lap until they re-encounter each other in the 4th frame, with the secondary wave (the counter-clockwise wave) decreasing significantly between intersections. Upon meeting each other, the luminosity at the intersection increases sharply, after which the cycle repeats with the pattern of collision, separation, decay, and collision again.

In order to better display and analyze the mode of operation and present temporally varying effects, the high-speed videos are post-processed further. It was observed that the high impulse hot jet impinging on the mirror induces vibrations that may cause the combustor annulus location within the video frame to shift over time. In order to remove this shift, an image detection algorithm was implemented to identify and track the combustor annulus from frame to frame. Based on the combustor trajectory, each frame was re-centered, yielding a steady frame of reference for further processing. At the same time, the inner and outer perimeter of the combustor annulus are identified. As an example, Fig. 5a shows a centered frame of the previously discussed single wave case. It clearly shows a single wave propagating clockwise. The two dashed white circles show the inner and outer radius of the annulus, as determined by the algorithm. In order to account for uncertainty in the annulus detection, both radii are slightly expanded, as indicated by the solid white circles. In a next step, the luminosity data within the expanded annulus is extracted at an angular resolution of 1° around the perimeter and unwrapped for each frame of the video, as demonstrated in Fig. 5b. The angular position is increasing in the clockwise direction, starting at the top of the frame, as indicated in

Fig. 5a. The extracted image is then averaged along the radial dimension to obtain one scalar value representing the luminosity strength within the combustor annulus at a given time and location. The resulting angular luminosity distribution is plotted in Fig. 5c. It clearly shows a steep luminosity peak propagating in clockwise direction (in positive angular direction), followed by a much longer decaying luminosity trailing tail.

The average luminosity as a function of the angular position is then combined and stacked up with the same procedure applied to each frame, yielding the space-time (X-t) diagram as shown in Fig. 6a. In order to extract the number, direction and speed of waves, the slopes and positions of the luminosity traces are identified using a Hough transform. The individual steps necessary are demonstrated in Fig. 6 for a subset of 10 consecutive wave laps. First, the X-t diagram is converted to a binary black and white image (BW), as shown in Fig. 6b. Based on the BW conversion, the image is reduced to a set of single pixel width lines located at the rising edge, as shown in Fig. 6c. A Hough transform is performed on the leading edge line segments to retrieve the luminosity characteristics, defined by their slope angle and position. A sub-section of the resulting Hough transform for the given example case is shown in Fig. 6d. It describes the length ρ and angle θ of a straight line drawn from the image root (at 0° for the first frame in the X-t diagram) perpendicular to a detected line segment. The peaks in the Hough transform correspond to the luminosity characteristics as the most prominent lines present in the X-t diagram and their slope angles and distances from the image root are marked with red circles. The luminosity characteristic's slope angle can easily be converted to a lap-
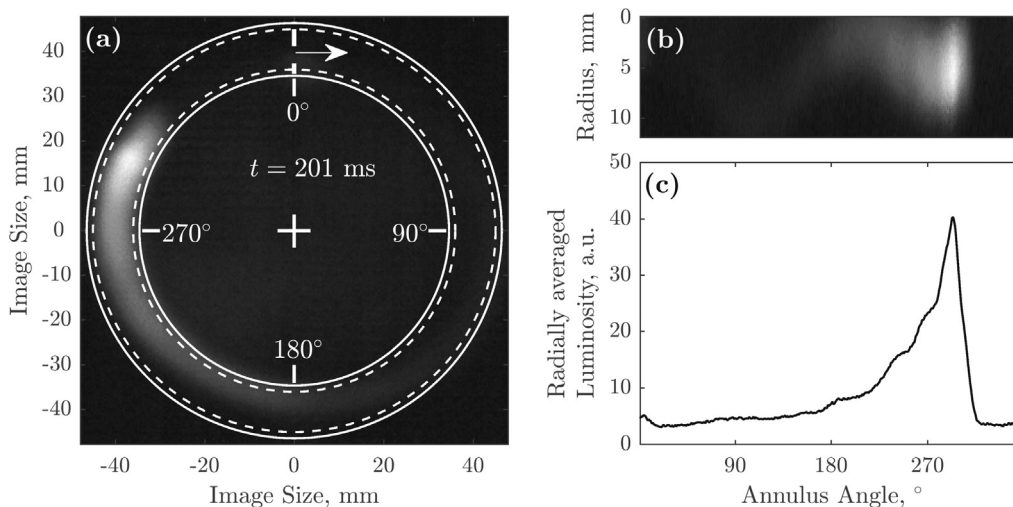

Fig. 5. Video frame post-processing example for a single wave propagating clockwise, at a time of 201 ms into the run. The luminosity within the range marked by the white circles in the centered frame (a) is extracted and unwrapped (b) (angular position is increasing in clockwise direction, starting at the top, as shown in (a)), and finally averaged along the radius (c).
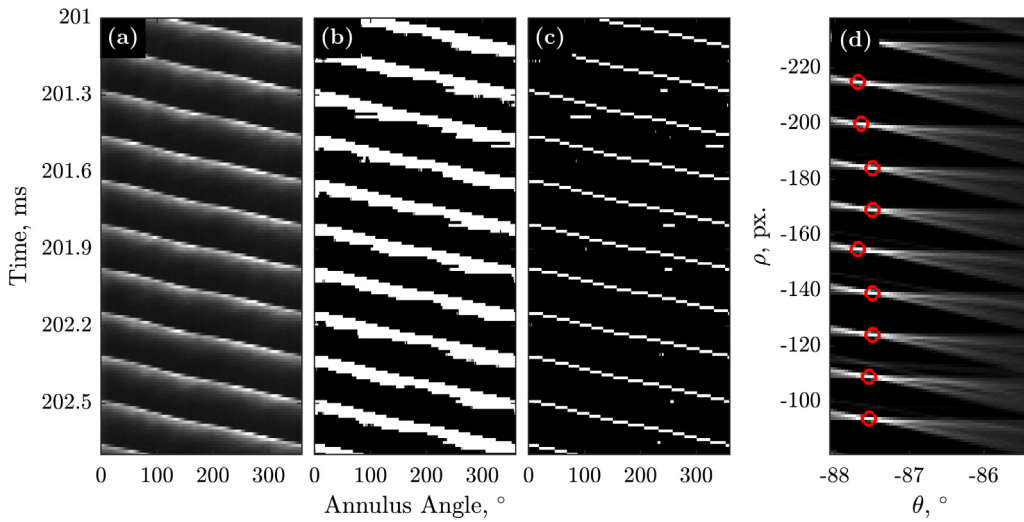
Fig. 6. Luminosity characteristics detection process. The radially-averaged luminosity for each frame is combined (a), converted to black and white (b), and the leading edges of the luminosity traces (c) are detected. A hough transform based on the leading edges reveals significant peaks (marked with red circles), which correspond to luminosity characteristics with a slope θ, which is converted to wave speed. (For interpretation of the references to colour in this figure legend, the reader is referred to the web version of this article.)

averaged wave speed $\bar{v}$, knowing the camera frame rate F_s and the RDC annulus mean perimeter P_m, using Eq. (1). The factor $1/360$ corresponds to a full lap around the combustor annulus at a mean perimeter of P_m.

$$\bar{v} = \frac{|\tan(\theta)|F_s P_m}{360} \tag{1}$$

For the single wave case shown in Fig. 7a, one can clearly see the steady propagation of the wave from left to right (clockwise) as the time increases (top to bottom). This is consistent with the results of the pressure traces discussed in Fig. 2. One example selected luminosity characteristic is shown with the orange line in Fig. 7a, however this approach is able to identify each lap of the wave for the duration of the test run. Each lap of the wave is then given a time stamp corresponding to the time in the middle of the line (shown by the square marker in Fig. 7a). The wave speeds are calculated based on Eq. (1) and can then be plotted as shown in Fig. 7b as orange triangle markers. Here, a subset of the measurements is plotted for slightly more than 15 ms. Also plotted here is a moving average of 10 measurements (solid black line) and the wave speed as determined by the dominant mode in the short time FFT of PCB 06 (blue circle markers). Good agreement exists between the moving average and the PCB measurements, however much more lap-to-lap variation can be observed in the speed of the wave as measured by the characteristics. In measuring the wave speed using the Hough transform, there exists uncertainty in the measured velocity that is between ± 30 and ± 50 m/s at the low and high ends of the measured velocity range, respectively. This level of uncertainty is comparable with the short time FFT, however with much higher temporal resolution (the FFT uses a sliding window of 10 ms, which corresponds to

approximately 40–50 laps of the detonation wave in this mode of operation). Based on the entire video recording from 0.2 to 0.234 s and the detected luminosity characteristics the average wave speed was found to be $\bar{v} = 1488$ m/s with a standard deviation of 40 m/s.

This process is repeated for the second example described in Fig. 4 for two counter-rotating waves. Shown in Fig. 8, the crossing streak patterns again clearly show the presence of two steady waves rotating in opposite directions. Applying the same Hough transform process described above to identify the propagation of a wave in the X-t space, the lap-averaged speed of each wave can be identified. Shown in Fig. 8a, the clockwise and counter-clockwise waves are identified with example characteristics shown in orange and yellow, respectively. Following the same procedure as before, the lap-averaged velocities are plotted in Fig. 8b along with the moving averages and wave speeds determined from the FFT. Starting from the example crossing point of the characteristics in Fig. 8a marked with a blue square, one can see that the crossing points shift from lap-to-lap, moving clockwise over the shown duration. In that time, the crossing point near 180° shifts to approximately 255°. The average lap speeds of the counter-clockwise and clockwise waves are 1113 m/s and 1174 m/s, with standard deviations of 39 m/s and 29 m/s, respectively. The individual wave speeds for each lap in Fig. 8a show significant variation of the individual lap speeds over time. These fluctuations are much greater than what can be observed by the short-time FFT. As shown in Fig. 3c, the FFT of the pressure sensor time series for this case also clearly shows the presence of two waves at separate frequencies in the spectrum that are in good agreement with the wave speeds derived from the characteristics. However, by only decreasing the FFT frequency resolution marginally
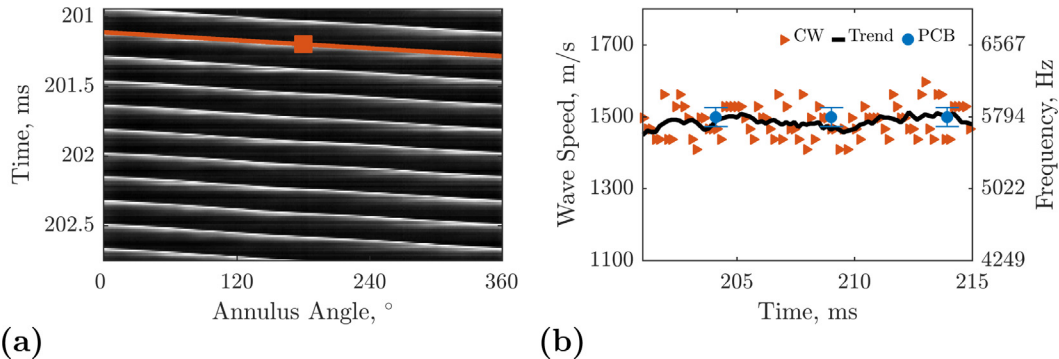

(a)

(b)

Fig. 7. (a) Radially-averaged luminosity within the RDC annulus plotted over annulus angle and run time, together with a single measured sample characteristic path line, showing stable one-wave propagation in clockwise direction. (b) Detonation wave speed for a subset of laps, together with moving average trend and the dominant short-time FFT mode of PCB 06 show an overall very good agreement of the two approaches.
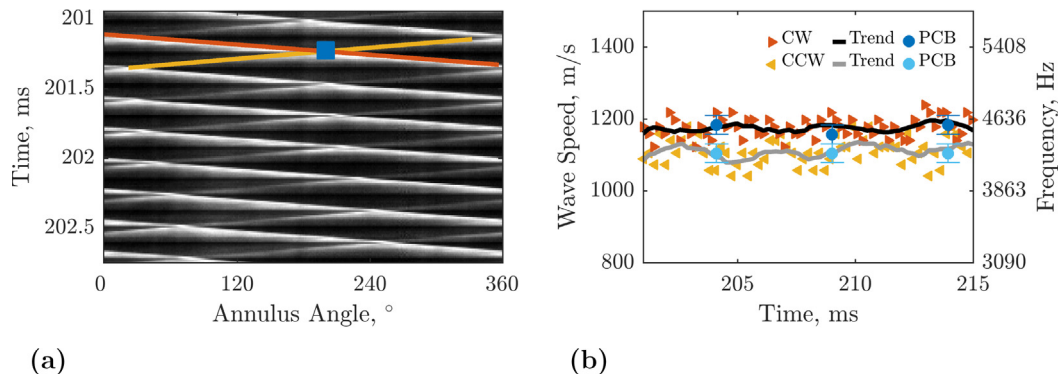
Fig. 8. Radially-averaged luminosity within the RDC annulus (a), showing stable operation with two counter-rotating waves. Counter-clockwise waves follow the yellow path and the orange sample characteristic showing waves going in reverse direction. (b) Detonation wave speed for a subset of laps, as calculated based on the luminosity characteristics of both waves, together with their moving average and the two short-time FFT dominant peaks of PCB 06. (For interpretation of the references to colour in this figure legend, the reader is referred to the web version of this article.)

both peaks were observed to merge into a single frequency peak, thereby effectively hiding the real operating mode of the RDC. As a result, the FFT-based analysis of the RDC operating mode from pressure signals requires a trade-off between sufficient temporal resolution to uncover operating dynamics and fine enough frequency resolution to detect the real operating mode. The clockwise shift of the intersection point observed in the time period shown in Fig. 8a due to the faster clockwise propagating wave can also be seen in the individual lap and moving average wave speeds shown in Fig. 8b.

The mean luminosity profile for the single wave case can be obtained by shifting the luminosity images in Fig. 7 into the wave's frame of reference. This is done by following the identified characteristic as an indicator of the position of the wave. Aligning the individual frames as shown in Fig. 9a, one can observe the evolution of the wave over its lifetime. From this figure where the wave is moving from left to right, the luminosity profiles show an apparently stochastic fluctuation in both extent and brightness over time. Averaging these profiles, the normalized mean luminosity is plotted in Fig. 9b in the solid line with the standard deviation at each angular position also plotted in the dashed lines. The mean profile shows that, on average, the detonation wave shows a sharp increase in luminosity within approximately 40° of the annulus perimeter and a much longer tail extending through approximately 180° of the annulus perimeter. Additionally, at the peak luminosity, the intensity fluctuates by up to ±20% of the mean luminosity.

Based on the identified characteristics in the single wave cases, the phase of individual pressure measurements relative to the position of the wave as detected in the natural luminosity could also be determined. By plotting the pressure measurements as a function of the phase relative to the luminosity, the mean averaged pressure distribution around the combustor annulus can be determined. Fig. 10 shows a scatter plot of the pressure measurements from four different pressure sensors in the wave frame of reference. One can see that the pressure distribution for each of the sensors collapses nicely, which allows for the averaged profile to be determine and plotted in the solid black line with variations of plus or minus one standard deviation shown in the dashed lines.

From this approach, the natural luminosity and mean pressure distribution through the wave can be compared, as shown in Fig. 11. Care should be given in interpreting these results, however, as the exact phase between the averaged pressure and natural luminosity is dependent on the edge finding algorithm which determines the characteristics. Combined with long exposure times compared with the pressure data acquisition rate, there is some uncertainty in the precise positioning of the two averages relative to one another and the two are plotted with an arbitrary phase difference here.

In Fig. 11a, it can been seen that increasing the mass flow rate of combustion air for a constant equivalence ratio results in a one-to-one increase in the peak height for both the pressure and natural luminosity averages. Interestingly, the shapes and widths of the wave are quite similar between the two different measurements. In Fig. 11b, the equivalence ratio is varied for a constant combustion air mass flow rate of 0.30 kg/s. For all of the different equivalence ratios, the pressure profile is quite consistent, with approximately equal peak pressures. However, the natural luminosity shows the highest values for
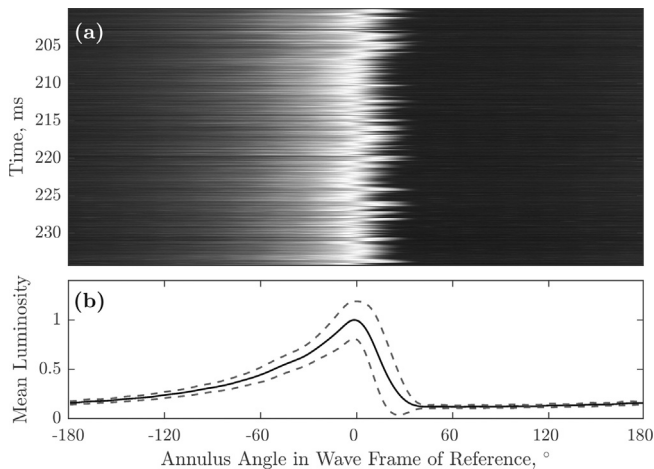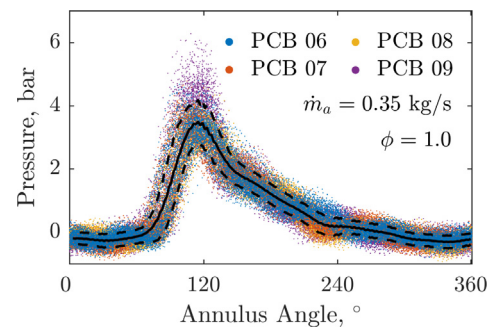

Fig. 9. Single wave mean luminosity in annulus over time, shifted along the wave characteristic, aligned at the center of the annulus mean perimeter. Wave is propagating from left to right. Bottom shows the average luminosity (solid line), with one standard deviation (dashed lines).

Fig. 10. Pressure measurements aligned into the wave frame of reference for 0.35 kg/s, phi = 1.0 for four distributed pressure sensors. The mean pressure distribution is plotted in solid black, with the dashed black lines indicating plus or minus one standard deviation from the mean.
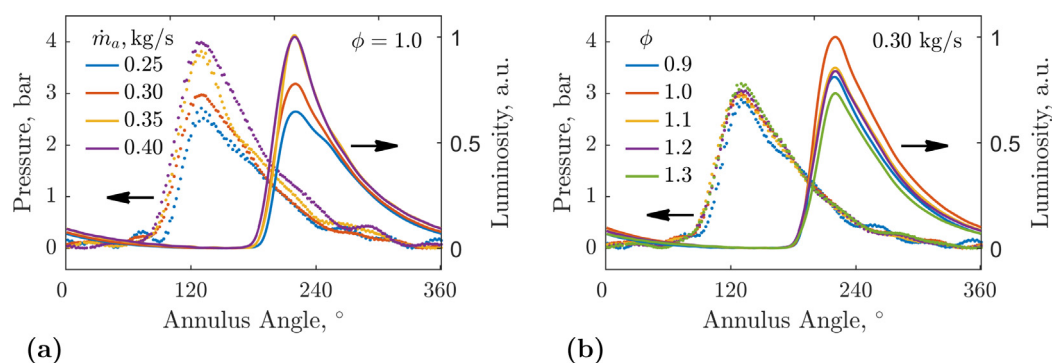
Fig. 11. Synchronized, average luminosity and pressure profiles for (a) varying combustion air mass flow rates at stoichiometric condition, and (b) varying equivalence ratio at 0.30 kg/s combustion air mass flow rate.
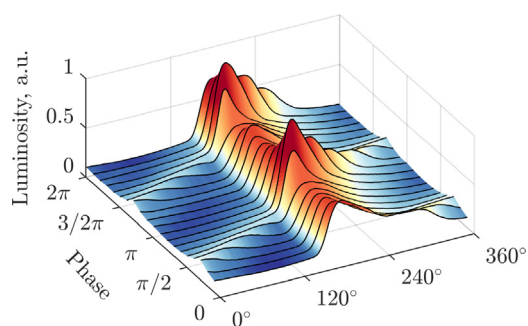

Fig. 12. Phase averaged mean luminosity locked on the primary wave frame of reference.

stoichiometric conditions and decreases for leaner and richer conditions.

Fig. 12 shows the phase averaged mean luminosity in the case with two counter-rotating waves. The frame of references is locked to the primary wave, and the phase average is conducted over the period spanning two intersections of the wave pair (which allows for the primary wave to complete approximately one complete lap of the annulus). Unfortunately, the measurement period is not long enough to provide an adequate amount of data to complete the phase averaging of the pressure traces in the same way as in Fig. 11, however much can still be learned from the natural luminosity. From this figure, one can clearly see the secondary wave propagating through the annulus, approaching the primary wave, interacting with the primary wave, and transiting through. When the secondary wave interacts with the primary wave, a sharp rise in the natural luminosity is observed, which then slowly decays over half the period until the two waves meet again on the opposite side. One important consideration that can be observed in this figure, is that the interaction of the two waves does not result in the instantaneous speeding up or slowing down of the primary wave. As the alignment of the frame of reference to the primary wave is determined by a characteristic with constant velocity which is fit to the entire lap of the wave around the annulus, the periodic slowing down of the wave in the course of a single period due to the interaction of the two waves would be visible in the phase average (the opposite is also true for an accelerated wave). Therefore, the two waves do appear to interact, as evidenced by the increased luminosity, however they pass without reflecting or disrupting the forward propagation of either wave.

4. Conclusion

This work has examined several different operating modes observed as the flow rate of reactant injection was varied in an RDC. Under each operating condition, pressure measurements distributed around the

perimeter of the annular combustion chamber observed and tracked the passage of pressure waves in either single wave or counter-rotating wave modes. Coupled with these measurements, high-speed imaging from the aft end of the combustor helped to identify the operating mode. Using these images, an approach for identifying the luminosity characteristic of the wave passage was presented. From these results, a number of conclusions could be drawn.

Above approximately 0.3 kg/s, a single rotating detonation wave was stabilized. As the flow rate was reduced below 0.25 kg/s, counter-rotating waves were stabilized which could be observed in the pressure time series as well as in their FFT spectrum. The counter-rotating waves propagated at different speeds, establishing a primary (faster) and a secondary (slower) wave, which resulted in the precession of the intersection points around the combustor. For each sensor, this rotation yielded a periodic oscillation of the measured pressure peak which corresponded to the difference in the frequencies of the two waves (beating frequency). It was also observed that the direction of the primary wave could sporadically switch directions, resulting in the reversal of the direction of the precessing intersection points. Finally, it was observed that the identification of this operating mode was facilitated by the close distribution of sensors within the combustor. From these results, it is likely that others have also observed these operating modes, however large sensor spacing has prevented the observation of an uninterrupted passage of each wave over a sensor pair which has obscured proper mode identification.

Analysis of the high-speed video showed significant fluctuations in the lap-to-lap speed of the single wave mode, with a standard deviation in measured wave speed of 40 m/s. It was also shown that this approach is capable of providing much higher temporal resolution of wave speed (relative to spectral techniques like the FFT of the pressure signals) while also clearly identifying the wave direction. These benefits were highlighted in the analysis of the counter-rotating wave mode where the different wave speeds were clearly distinguished and their precessing intersecting points were easily identified.

An additional benefit of identifying the position of the wave as it propagates around the combustion annulus is the ability to lock the measurements of natural luminosity and pressure into the wave's frame of reference. From this analysis, the profile of average wave luminosity for varying reactant flow rates was identified. It was observed that the strength and breadth of the luminosity peak is a stronger function of the reactant mass flow rate than the equivalence ratio. This approach also allowed for the transformation of the measured pressure from distributed pressure sensors to be combined into an averaged pressure profile through the wave. By this analysis, it was observed that the average pressure profile closely mirrored the luminosity with varying reactant mass flow rate, however the mean pressure profile was largely independent of the global equivalence ratio.

Lastly, the phase-averaged luminosity in the case of counter-rotating waves was examined from the frame of reference of the primary wave.

Here it was observed that the weaker, secondary counter-rotating wave would transit through the primary wave. At the point of intersection, both waves were quickly strengthened followed by a slower decay in luminosity until subsequently meeting again. It was also observed here that the progression of neither wave was affected by their interaction, with neither wave exhibiting a periodic acceleration or deceleration at the point of interaction.

Conflict of interest

The authors declared that there is no conflict of interest.

Acknowledgements

References

[1] I.Q. Andrus, P.I. King, M.D. Polanka, F.R. Schauer, J.L. Hoke, Experimentation of a premixed rotating detonation engine utilizing a variable slot feed plenum, in: 54th AIAA Aerospace Sciences Meeting, January 2016, pp. 1–11.

[2] I.Q. Andrus, P.I. King, M.D. Polanka, F.R. Schauer, J.L. Hoke, Design of a premixed fuel-oxidizer system to prevent flashback in a rotating detonation engine, in: 54th AIAA Aerospace Sciences Meeting, No. January, 2016, pp. 1–15.

[3] I.Q. Andrus, M.D. Polanka, F.R. Schauer, J.L. Hoke, Further experimentation of a premixed rotating detonation engine, in: 55th AIAA Aerospace Sciences Meeting, January 2017.

[4] D.A. Schwer, K. Kailasanath, Feedback into mixture plenums in rotating detonation engines, in: 50th AIAA Aerospace Sciences Meeting including the New Horizons Forum and Aerospace Exposition, January 2012, pp. 1–17.

[5] J.H.S. Lee, The Detonation Phenonmenon, 2nd ed., Cambridge University Press, Cambridge, 2008.

[6] J.H.S. Lee, R. Knystautas, A. Freiman, High speed turbulent deflagrations and transition to detonation in H2air mixtures, Combust. Flame 56 (2) (1984) 227–239.

[7] R.M. Russo, Operational Characteristics of a Rotating Detonation Engine Using Hydrogen and Air, Ph.D. thesis, 2011.

[8] V. Anand, A.C. St. George, R.B. Driscoll, E.J. Gutmark, Experimental Investigation of H2-air mixtures in a rotating detonation combustor, in: Proceedings of ASME Turbo Expo 2015: Turbine Technical Conference and Exposition, 2015, pp. 1–13.

[9] X. Han, S. Zhang, J. Wang, Experimental investigation on rotating detonation engine with different mixing distance, in: 52nd AIAA/SAE/ASEE Joint Propulsion Conference, 2016, pp. 1–6. URL http://arc.aiaa.org/doi/10.2514/6.2016-4924.

[10] F.A. Bykovskii, S.A. Zhdan, E.F. Vedernikov, Continuous detonation of fuel-air mixtures, Combust. Explos. Shock Waves 42 (4) (2006) 463–471.

[11] F.A. Bykovskii, S.A. Zhdan, E.F. Vedernikov, Continuous spin detonations, J. Propul. Power 22 (6) (2006) 1204–1216.

[12] J. Kindracki, A. Kobiera, P. Wolański, Z. Gut, M. Folusiak, K. Swiderski, Experimental and numerical study of the rotating detonation engine in hydrogen-air mixtures, Progress Propuls. Phys. 2 (2011) 555–582.

[13] S.M. Frolov, A.V. Dubrovskii, V.S. Ivanov, Three-dimensional numerical simulation of the operation of the rotating-detonation chamber with separate supply of fuel and oxidizer, Russian J. Phys. Chem. B 7 (1) (2013) 276-35–276-43.

[14] R.B. Driscoll, P. Aghasi, A.C. St. George, E.J. Gutmark, Three-dimensional, numerical investigation of reactant injection variation in a H2/air rotating detonation engine, Int. J. Hydrogen Energy 41 (9) (2016) 5162–5175.

[15] R.B. Driscoll, A.C. St. George, E.J. Gutmark, Numerical investigation of injection within an axisymmetric rotating detonation engine, Int. J. Hydrogen Energy 41 (3) (2016) 2052–2063.

[16] T. Gaillard, D. Davidenko, F. Dupoirieux, Numerical simulation of a Rotating Detonation with a realistic injector designed for separate supply of gaseous hydrogen and oxygen, Acta Astronaut. 141 (August) (2017) 64–78.

[17] C.A. Nordeen, D.A. Schwer, F.R. Schauer, J.L. Hoke, T. Barber, B.M. Cetegen, Role of inlet reactant mixedness on the thermodynamic performance of a rotating detonation engine, Shock Waves 26 (4) (2015) 417–428.

[18] F.A. Bykovskii, S.A. Zhdan, E.F. Vedernikov, Continuous detonation in the regime of nonstationary ejection of the oxidizer, Dokl. Phys. 54 (1) (2009) 29–31.

[19] J.A. Suchocki, S.-T.J. Yu, J.L. Hoke, A.G. Naples, F.R. Schauer, R.M. Russo, Rotating detonation engine operation, in: 50th AIAA Aerospace Sciences Meeting including the New Horizons Forum and Aerospace Exposition, January 2012, pp. 1–11.

[20] S.W. Theuerkauf, F.R. Schauer, R. Anthony, J.L. Hoke, Experimental characterization of high-frequency heat flux in a rotating detonation engine, in: 53rd AIAA Aerospace Sciences Meeting, January 2015, pp. 1–10.

[21] F. Chacon, M. Gamba, Development of an optically accessible continuous wave Rotating Detonation Engine, 2018 Joint Propulsion Conference, 2018.

[22] R. Bluemner, M.D. Bohon, C.O. Paschereit, E.J. Gutmark, Single and counter-rotating wave modes in an RDC, in: 56th AIAA Aerospace Sciences Meeting, no. January, Kissimme, FL, 2018, pp. 1–10. URL https://arc.aiaa.org/doi/10.2514/6.2018-1608.

[23] R. Bluemner, M.D. Bohon, C.O. Paschereit, E.J. Gutmark, Dynamics of counter-rotating wave modes in an RDC, in: 54th AIAA/SAE/ASEE Joint Propulsion Conference, 2018.

[24] A. Roy, D.H. Ferguson, T. Sidwell, B. O'Meara, P. Strakey, C. Bedick, A. Sisler, Experimental study of rotating detonation combustor performance under preheat and back pressure operation, in: 55th AIAA Aerospace Sciences Meeting, January 2017, pp. 1–16.

[25] L. Deng, H. Ma, C. Xu, X. Liu, C. Zhou, The feasibility of mode control in rotating detonation engine, Applied Thermal Engineering.

[26] J.W. Bennewitz, B.R. Bigler, W.A. Hargus, S.A. Danczyk, R.D. Smith, Characterization of detonation wave propagation in a rotating detonation rocket engine using direct high-speed imaging, in: 2018 Joint Propulsion Conference, 2018, pp. 1-22.

[27] B.A. Rankin, D.R. Richardson, A.W. Caswell, A.G. Naples, Imaging of OH* chemiluminescence in an optically accessible nonpremixed rotating detonation engine, in: 53rd AIAA Aerospace Sciences Meeting, No. January, Kissimmee, FL, 2015, pp. 1–16.

[28] B.A. Rankin, D.R. Richardson, A.W. Caswell, A.G. Naples, J.L. Hoke, F.R. Schauer, Chemiluminescence imaging of an optically accessible non-premixed rotating detonation engine, Combust. Flame 176 (2017) 12–22.

[29] P.A.T. Cocks, A.T. Holley, High fidelity simulations of a non-premixed rotating detonation engine, in: 54th AIAA Aerospace Sciences Meeting, No. January, 2016, pp. 1–18.

[30] B.A. Rankin, C.A. Fugger, D.R. Richardson, K.Y. Cho, J.L. Hoke, A.W. Caswell, J.R. Gord, F.R. Schauer, Evaluation of mixing processes in a non-premixed rotating detonation engine using acetone PLIF, in: 54th AIAA Aerospace Sciences Meeting, No. January, 2016, pp. 1–12. URL http://arc.aiaa.org/doi/10.2514/6.2016-1198.

[31] J.C. Shank, Development and testing of a rotating detonation engine run on hydrogen and air, Ph.D. thesis, Air Force Institute of Technology, 2012.

[32] S. Gordon, B.J. McBride, Computer Program for Calculation of Complex Chemical Equilibrium Compositions and Applications, 1996.

[33] Q. Xie, H. Wen, W. Li, Z. Ji, B. Wang, P. Wolanski, Analysis of operating diagram for H2/Air rotating detonation combustors under lean fuel condition, Energy 151 (2018) 408–419.

[34] W. Lin, J. Zhou, S. Liu, Z. Lin, An experimental study on CH4/O2 continuously rotating detonation wave in a hollow combustion chamber, Exp. Thermal Fluid Sci. 62 (2015) 122–130.

[35] V. Anand, A.C. St. George, E.J. Gutmark, Amplitude modulated instability in reactants plenum of a rotating detonation combustor, Int. J. Hydrogen Energy (2017) 1–16.

[36] R.W. Schefer, W.D. Kulatilaka, B.D. Patterson, T.B. Settersten, Visible emission of hydrogen flames, Combust. Flame 156 (6) (2009) 1234–1241.